Birefringent phase demodulator: application to wave plate characterization

F. E. Veiras,[1,2,3,*] L. M. Riobó,[4] C. L. Matteo,[1,3] L. I. Perez,[5,6] and M. T. Garea[4]

[1]Laboratorio de Sistemas Líquidos–GLOmAe, Departamento de Física, Facultad de Ingeniería, Universidad de Buenos Aires, Av. Paseo Colón 850, CABA, Buenos Aires C1063ACV, Argentina

[2]Electrónica e Informática, Instituto Nacional de Tecnología Industrial, P.O. Box B1650WAB, B1650KNA San Martín, Argentina

[3]CONICET, Av. Rivadavia 1917, CABA C1033AAJ, Argentina

[4]Laboratorio de Aplicaciones Ópticas–GLOmAe, Departamento de Física, Facultad de Ingeniería, Universidad de Buenos Aires, Av. Paseo Colón 850, CABA, Buenos Aires C1063ACV, Argentina

[5]Laboratorio Láser–GLOmAe, Departamento de Física, Facultad de Ingeniería, Universidad de Buenos Aires, Av. Paseo Colón 850, CABA C1063ACV, Argentina

[6]INTECIN–CONICET, Av. Paseo Colón 850, CABA C1063ACV, Argentina

*Corresponding author: fveiras@fi.uba.ar

Received 5 January 2015; revised 12 February 2015; accepted 12 February 2015; posted 17 February 2015 (Doc. ID 231604); published 16 March 2015

The scope of this work is to present a phase demodulator that enables the recovery of temporal phase information contained in the phase difference between two signals with different polarizations. This demodulator is a polarization interferometer that may consist only of a uniaxial crystal slab and a polarizer sheet. The phase shift between two orthogonal components of the electric field is translated into space by means of birefringent crystals, which act as demodulators or phase analyzers with great robustness. The experimental scheme utilized is based on a simple conoscopic interference setup. Each portion of the space in which the interference pattern is projected contains not only the unknown temporal phase we want to recover, but also a phase shift due to the uniaxial crystal itself. The underlying idea is developing simultaneous phase shifting with uniaxial crystals. Thus, different phase recovery techniques can be applied in order to maximize their ability to track high-speed signals. Depending on the characteristics of the fringe pattern, it will permit phase recovery via different classical procedures. In order to prove the demodulator under different experimental and signal processing schemes, we employed it for wave plate characterization. The results obtained not only allow some wave plate features such as axes determination and retardance to be characterized, but also prove the working principle and capabilities of the demodulator.

OCIS codes: (120.2650) Fringe analysis; (120.3180) Interferometry; (120.5050) Phase measurement; (230.5440) Polarization-selective devices; (260.1180) Crystal optics; (260.1440) Birefringence.

http://dx.doi.org/10.1364/AO.54.002326

1. Introduction

There are different purposes and methods for phase modulation. In fact, several elements can be used as phase shifters in a wide range of devices and experiments. For instance, when working with polarized light, polarization states can be changed by retarders that introduce phase shifts between orthogonal components of the electric field [1].

Generally speaking, interferometers translate different phenomena into spatio-temporal phase variations between their branches. By means of superposition, this gives rise to interferograms, i.e., intensity

1559-128X/15/092326-08$15.00/0

measurements. Depending on the complexity of the problem, it is possible to recover the phase information from one or more interferograms. Multiple experimental and signal processing techniques for recovering phase information have been developed. The wide range of purposes and experimental setups is also associated with the different processing techniques. When the phase information corresponds to space information associated with the shape of the wavefronts, the classical procedure corresponds to measuring the difference between a reference and a test wavefront. In other circumstances, the phase difference can be related to time-dependent phenomena such as vibrations, changes in the index of refraction, or any other phenomenon that alters the effective length of the branches of an interferometer. Nevertheless, the complexity of the problem may require the simultaneous determination of both time and space phase variations.

One of the highly studied problems corresponds to the interference of two superposed monochromatic beams. Regardless of the dependence of spurious external factors corresponding to space and time, the ideal case is represented by

$$I(\Delta\phi(\vec{\mathbf{r}},t)) = I_1 + I_2 + 2\sqrt{I_1 I_2}\,\cos\,\Delta\phi(\vec{\mathbf{r}},t). \quad (1)$$

This way, the intensity variations only depend on the phase difference between both beams $\Delta\phi(\vec{\mathbf{r}},t)$. Based on the experimental setup, this phase may depend on both time and space. There are several techniques that allow the recovery of the phase information included in $\Delta\phi(\vec{\mathbf{r}},t)$ by means of intensity measures $I(\Delta\phi(\vec{\mathbf{r}},t))$. Some of the most extensively used correspond to the so-called Fourier-transform method (FTM) [2] and phase shifting interferometry (PSI) [3]. Both of them are based on the introduction of controlled phase shifts between the branches of an interferometer. In general, it is possible to implement any of them to determine space- or time-dependent unknown phases. Throughout this work, we show how to introduce space-dependent phase shifts with uniaxial crystals in order to recover temporal phase information. This temporal phase information is associated with the phase difference between two orthogonal components of the electrical field, v and h. It is known that the phase shift introduced between two orthogonal components of the electric field changes when light from a monochromatic polarized source goes through a rotating a wave plate. Such variations depend on the azimuth angle and permit the introduction of phase shifts between the branches of a polarization interferometer. This interferometer may only consist of a single crystal plate and a polarizer sheet [4]. As a result, the fringe pattern of the space interferograms moves according to the phase shift between components [5]. Here, we explain how this movement of the fringe pattern allows us to identify both the fast axis and the slow axis of a plate retarder and determine its retardance. We propose that the waves associated with orthogonal components (v and h) of the electric field may be introduced in a polarization interferometer in order to recover any unknown phase information $\Delta\phi_{v-h}(t)$. Moreover, due to the different phase topologies over the space interferograms obtained by means of conoscopic interference with uniaxial crystals we show that different techniques for phase recovery can be implemented.

First, we present a basic conoscopic interference setup and some results that would help to understand the topology of the phase for different uniaxial crystals. Second, we show two classical phase recovery techniques implemented with uniaxial crystals. In order to compare both techniques, we employed them in wave plate characterization. We present the experimental results and finally the conclusions.

2. Conoscopic Interference Patterns

Diverse experimental techniques have been used for the characterization of birefringent crystals. One of them corresponds to interferometry with converging or diverging beams that go through a crystalline sample. This technique and its variants can be employed for proper crystal characterization [6–9], as part of a device [10–12], or in different lab experiments [13]. In this section, we propose that two orthogonal components of the electric field, v and h, are introduced in a polarization interferometer in order to analyze their phase difference. In a simple interferometer, constituted by a plane-parallel plate with principal refractive indices n_o and n_e, it is possible to associate these two components of the electric field with the ordinary and extraordinary refracted beams. This way, a polarization interferometer gives rise to a fringe pattern from these components of the electric field. In the conoscopic setup of Fig. 1, the impinging beam is expanded and transmitted through a plane-parallel uniaxial plate of thickness H. This can be achieved by grounding the first interface of the crystal located at $x = 0$. Fringes can be observed over a detection plane of coordinates (x_D, y, z) if an analyzer is placed adequately after the crystal. That is, this interferometer yields to a spatial fringe pattern or interferogram by means of the addition of

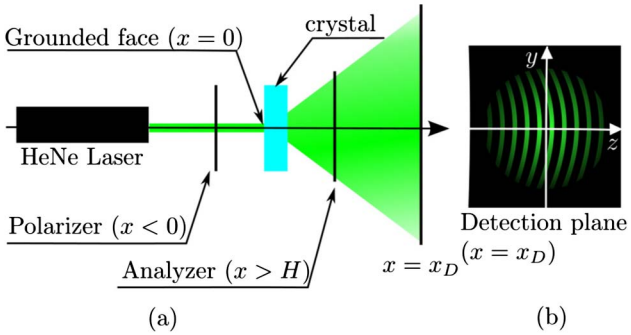

Fig. 1. Basic conoscopic setup. The detection plane is perpendicular to the direction of propagation of the beam (x). (x, y, z) is the frame associated with the crystal plate where z corresponds to the projection of the optical axis over the first interface. The crystal plate is placed with the z axis horizontal. The polarizer and the analyzer could be either parallel or perpendicular. For better fringe visibility they should hold an angle of $\pm 45°$ with regard to the horizontal axis.

a phase difference between the ordinary and extraordinary beams $\Delta\phi_{o-e}(x_D, y, z)$. Different approximations have been developed for expressing this phase shift [4]. However, for the conceptual and design purposes of this work, the second-order approximations are enough. Thus, if the crystal plate is oriented with its optical axis parallel to the horizontal plane (x, z), the expression of the phase shift is

$$\Delta\phi_{o-e}(x_D, y, z) \simeq \frac{2\pi H}{\lambda_v}\left(A + n\frac{B}{|x_D|}z + n^2\frac{C_Y}{x_D^2}y^2 + n^2\frac{C_Z}{x_D^2}z^2\right), \quad (2)$$

where A, B, C_Y, and C_Z are

$$A = n_o - \frac{n_o n_e}{(n_o^2\cos^2\theta + n_e^2\sin^2\theta)^{\frac{1}{2}}}, \quad (3)$$

$$B = \frac{(n_o^2 - n_e^2)\sin\theta\cos\theta}{(n_o^2\cos^2\theta + n_e^2\sin^2\theta)}, \quad (4)$$

$$C_Y = \frac{n_o^2 - n_e(n_o^2\cos^2\theta + n_e^2\sin^2\theta)^{\frac{1}{2}}}{2n_o n_e(n_o^2\cos^2\theta + n_e^2\sin^2\theta)^{\frac{1}{2}}}, \quad (5)$$

$$C_Z = \frac{n_o^2 n_e - (n_o^2\cos^2\theta + n_e^2\sin^2\theta)^{\frac{3}{2}}}{2n_o(n_o^2\cos^2\theta + n_e^2\sin^2\theta)^{\frac{3}{2}}}, \quad (6)$$

and where θ corresponds to the angle between the optical axis and the interfaces of the crystal. According to these expressions, as explained in [4], the distribution of the phase over the detector plane holds constant-phase lines that follow a conic equation. Depending on the characteristics of crystal, the center and type of the conic may vary. For a given crystal material, the topology of the phase depends on the direction of the optical axis θ, i.e., the crystal cut. In the case of large distances between the center of the conic and the origin $(y = 0; z = 0)$, it might be practically impossible to visualize the center on the plane (x_D, y, z). Such is the case of a quartz plane-parallel plate ($n_o = 1.5426$, $n_e = 1.5516$) of thickness $H = 3$ mm with its optical axis at approximately $\theta = 45°$ from its faces. The constant-phase lines are elliptical, but the displacement of the center of the ellipses is too far for visualization (Fig. 2).

This fringe distribution is often pursued in traditional interferometric schemes, such as Michelson or Mach–Zehnder interferometers. In those cases, the so-called tilted fringes are obtained by tilting a mirror. This way, the images of the source through each of the two branches are misaligned with the mean direction of propagation of the emerging beams. In the case of uniaxial crystal interferometers, when $\theta \neq 0°$ and $\theta \neq 90°$, the extraordinary image is laterally displaced in the z direction whereas the ordinary image remains attached to the x axis. For quartz, this lateral displacement reaches its maximum when θ is closer to 45° and the phase shift between the ordinary and extraordinary beams over the detection plane is

$$\Delta\phi_{o-e}(x_D, y, z) \approx \frac{2\pi H}{\lambda_v}\left(A + n\frac{B}{|x_D|}z + n^2\frac{C_Y}{x_D^2}y^2\right). \quad (7)$$

This way, it is possible to obtain interferograms with high spatial frequency in the z direction. Beyond the specific distribution of the phase $\Delta\phi_{o-e}(x_D, y, z)$ over the plane, it is important to highlight the stability of this phase against external factors. This is due to the interferometric setup, which consists of a common path polarization interferometer. For such an interferometer, its branches are superposed in space but only separated by their polarization and therefore undergo the same ambient perturbations. The uniaxial crystal splits the incident beam into two polarized beams: the ordinary and the extraordinary beams. The stability of the phase shift introduced depends on its crystalline structure. Furthermore, the grounded face of the crystal that expands the impinging beam eases the alignment process and also provides stability.

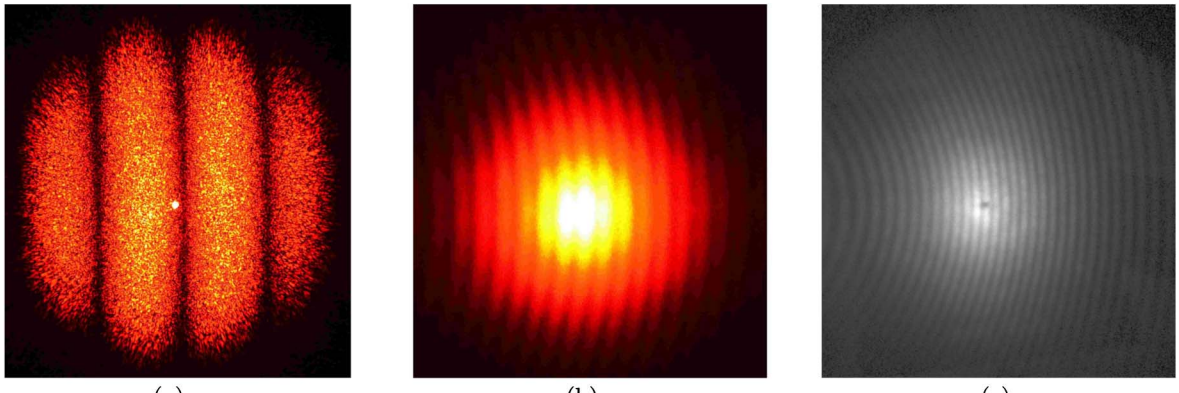

(a) (b) (c)

Fig. 2. Interference fringes obtained with a quartz crystal plate. Crystal parameters (approximated values): $\theta = 45°$, $n_o = 1.5426$, $n_e = 1.5516$, and $H = 3$ mm. We illuminate the grounded face of the crystal with a He–Ne laser ($\lambda_v = 632.8$ nm). Different captures of the interference pattern: (a) direct observation with a camera plus objective. (b) Rear projection diffusing screen. (c) Rear projection diffusing screen plus mask (dark dot).

This way, if we place the uniaxial crystal plate that constitutes the interferometer with its y axis vertical and z axis horizontal, we can associate the v and h components of the beam that impinge on the grounded face with the ordinary beam (vertical component) and with the extraordinary beam (horizontal component). This experimental setup allows us to place a phase modulator between the first polarizer and the crystal plate (Fig. 1). This phase modulator introduces a time-dependent phase shift $\Delta\phi_{v-h}(t)$ between the components of the field associated with v and h polarizations before impinging on the first interface of the crystal plate.

3. Phase Recovery Techniques with Uniaxial Polarization Interferometers

There are many different phase recovery or demodulating techniques based on the introduction of a controlled phase difference between the branches of an interferometer. This phase shift introduced can be dependent on time or space according to the experiment. Regardless of the functional dependence of the unknown phase to recover (time and/or space), the phase shift introduced might also be a function of space and/or time. However, if we are dealing with an unknown time-dependent phase, the introduction of a time-dependent phase would result in requiring an increased time resolution and bandwidth of the photodetectors (i.e., faster photodetectors). The consequences are similar if we are dealing with a space-dependent unknown phase. In this case, the introduction of a space-dependent phase would result in requiring increased spatial resolution and bandwidth of the photodetectors (i.e., increased number of photodetectors). For an unknown time-dependent phase, if we instead employ the introduction of a space-dependent controlled phase, the time and bandwidth requirements of the detection system would not be increased by the introduction of the controlled phase. However, the number of photodetectors would have to be increased in order to track the additional spatial information introduced.

The stability of the controlled phase difference introduced is a very important parameter in these demodulation schemes. Since we are dealing with a time-dependent unknown phase $\Delta\phi_{v-h}(t)$ (i.e., modulating phase) we introduce a controlled space-dependent phase whose time stability relies on the plane-parallel uniaxial plate, $\Delta\phi_{o-e}(x_D,y,z)$, described in the previous section. This way, over a plane of coordinates (x_D,y,z), from Eq. (1), $\Delta\phi(\vec{\mathbf{r}},t) = \Delta\phi_{o-e}(y,z) + \Delta\phi_{v-h}(t)$ and the interference equation can be rewritten as

$$I(y,z,t) = a(y,z) + b(y,z)\cos[\Delta\phi_{o-e}(y,z) + \Delta\phi_{v-h}(t)], \quad (8)$$

where $a(y,z)$ and $b(y,z)$ are respectively associated with the mean value and visibility of the fringe pattern over a plane located at $x = x_D$. After leaving the phase modulator, both signals share the same path until light reaches the photodiodes. As this is a common path interferometer, its branches are superposed. This feature also helps to mitigate error sources, since both of the branches are fixed together and exposed to the same noise sources. In order to recover the phase information $\Delta\phi_{v-h}(t)$, we propose two different approaches that employ a uniaxial crystal polarization interferometer as a phase demodulator. Both methods are based on the introduction of a space-controlled phase $\Delta\phi_{o-e}(y,z)$. However, they require different implementations, which lead to different performance regarding accuracy and velocity.

A. Spatial Carrier

It is relatively easy to recover phase information by means of the conoscopic interference patterns corresponding to a quartz plate with $\theta \approx 45°$. As pointed out in Section 2, the interferograms obtained by means of a quartz plate with its optical axis at 45° (Fig. 2) have a spatial frequency component. This frequency component is associated with the linear coefficient of Eq. (7) and acts as a carrier frequency for each y,

$$|k_{z0}| = \frac{2\pi H}{\lambda_v} n \left|\frac{B}{x_D}\right|. \quad (9)$$

This linear coefficient [Eq. (7)] associated with $\Delta\phi_{o-e}(y,z)$ is negative valued. This negative spatial frequency indicates that the phase $\Delta\phi_{o-e}(y,z)$ decreases along the z axis, from the concave to the convex [Figs. 2(b) and 2(c)]. This way, Eq. (8) becomes

$$I(y,z,t) = a(y,z) + b(y,z)\cos[k_{z0}z + \Delta\phi_{v-h}(t)]. \quad (10)$$

Equation (10) can be rewritten as

$$I(y,z,t) = a(y,z) + c(y,z,t)\exp(\mathrm{j}k_{z0}z) + c^*(y,z,t)\exp(-\mathrm{j}k_{z0}z), \quad (11)$$

where j corresponds to the imaginary unit and

$$c(y,z,t) = \frac{1}{2}b(y,z)\exp[\mathrm{j}\Delta\phi_{v-h}(t)]. \quad (12)$$

By applying the Fourier transform with respect to z in Eq. (11), we obtain for every value of y

$$\mathcal{I}(y,k_z) = \mathcal{A}(y,k_z) + \mathcal{C}(y,k_z - k_{z0}) + \mathcal{C}^*(y,k_z - k_{z0}) \quad (13)$$

and a spectrum such as the one in Fig. 3. The phase information is contained in either angle of the side bands (i.e., contained in $\mathcal{C}$ or $\mathcal{C}^*$). Interferograms like the ones shown in Figs. 2(b) and 2(c) can be analyzed by means of the Fourier transform. Those interferograms can be processed row by row, by means of the Fourier transform, which makes it possible to obtain a spectrum like the one depicted in Fig. 3.

Due to the symmetry properties of the Fourier transform of real signals, there are two side bands associated either with the positive carrier frequency (i.e., $\Delta\phi_{e-o}(y,z)$) or with the negative carrier frequency (i.e., $\Delta\phi_{o-e}(y,z)$). We would like to emphasize the fact that knowledge of the principal refractive

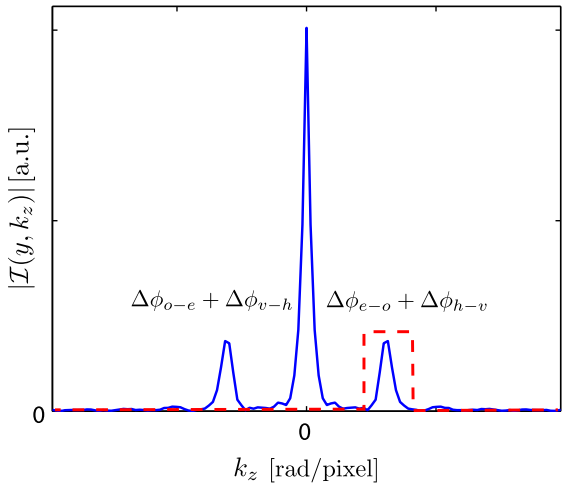

Fig. 3. Blue solid line, spectrum of a fringe pattern with a spatial frequency carrier k_{z0}; red dashed line, the filter applied.

indices and the orientation of the optical axis permits the determination of the phase information associated with each side band ($\mathcal{C}$ and $\mathcal{C}^*$) whose only difference is a minus sign ($\Delta\phi_{v-h}(t) = -\Delta\phi_{h-v}(t)$). By means of the filtering indicated in Fig. 3 it is possible to recover the phase information associated with $\mathcal{C}$ or $\mathcal{C}^*$. This way, the determination of $\Delta\phi_{v-h}(t)$ corresponds to the determination of the angle of the complex value $c(z)$ (or $c^*(z)$) [14].

As is known, speckle noise can be extremely detrimental in phase retrieving [15–18]. In order to improve the robustness of the postprocessing, we crop the interferograms to a portion where the fringes are almost vertical and calculate the average of the intensities along the columns [19–21]. Despite the fact that this averaging could diminish the visibility of the fringes, it allows us to obtain a clean spatial carrier k_{z0} without typical speckle noise. However, different filtering techniques and filters can be employed. Moreover, even the simplest techniques can be successfully employed due to the quality of the carrier. For every instant t the carrier frequency and the spectrum remain unaltered. Since the useful spectrum can be easily determined, it is possible to design a single filter for every t. All the processing operations could be performed by capturing a sequence of interferograms with a digital camera and a computer. Since the acquisition of the interferograms is performed by means of a digital camera, it can be somewhat slow for many applications. In the following subsection, we present a different processing technique that allows for much faster operation.

B. Spatial Phase Steps

If we place a single detector (e.g., a photodiode) at any point of the plane where the fringe patterns of Fig. 2 were recorded, the intensity measured would depend on its position (x_D, y_i, z_i) and time [Eq. (8)]:

$$I(x_D,y_i,z_i,t) = a(x_D,y_i,z_i) + b(x_D,y_i,z_i) \times \cos[\Delta\phi_{o-e}(x_D,y_i,z_i) + \Delta\phi_{v-h}(t)]. \quad (14)$$

This way, it is possible to find N fixed locations (x_D, y_i, z_i) for different photodiodes. The phase shift between the intensities, $I(x_D, y_i, z_i, t)$, makes it possible to recover the phase information $\Delta\phi_{v-h}(t)$ via a phase shifting algorithm for every t. The number of photodiodes N and the phase shift between any two of them $(\Delta\phi_{o-e}(x_D, y_i, z_i) - \Delta\phi_{o-e}(x_D, y_j, z_j))$ depends on the chosen algorithm. The phase differences are governed by $\Delta\phi_{o-e}$, which relies on the crystalline structure of the polarization interferometer.

There are several phase shifting algorithms to recover the phase $\Delta\phi_{v-h}(t)$. In particular, there is a solution that can be developed from the principle of least-squares estimation [22]:

$$\hat{\Delta}\phi_{v-h}(t) = \arctan\left[\frac{\sum_{i=1}^{N} n_i \tilde{I}(x_D,y_i,z_i,t)}{\sum_{i=1}^{N} d_i \tilde{I}(x_D,y_i,z_i,t)}\right]. \quad (15)$$

Both weighted summations of photodiode intensities in the numerator and denominator can be performed electronically and then acquired by means of a two-channel digital oscilloscope. Therefore, in a postprocessing stage, the arctangent can be calculated.

Since this technique requires significantly fewer photodetectors (in comparison with a digital camera), the acquisition of signals can be performed faster than in the previous scheme. However, the photodetectors have to be carefully located in order to achieve the desired phase shift.

In the following section, we propose an experiment with the purpose of comparing both techniques.

4. Characterization of a Wave Plate

Linear retarders such as wave plates introduce a phase shift between two privileged components of linearly polarized light. Commercial wave plates or other linear retarders, as well as *ad hoc* built prototypes, may have an incomplete specifications data sheet for a particular application. For example, their behavior might not be specified for a different wavelength, and/or the fast and slow axis marks may be missing. Usually, basic operation of linear retarders relies on the knowledge of these characteristics. They are of great interest for ellipsometry and for accurate polarization control. It is known that the retardance introduced between two orthogonal components of the electric field varies when a wave plate is rotated against a monochromatic light source. Such variations depend on the azimuth angle and allow the introduction of phase shifts between the branches of a polarization interferometer like the one described in Section 2. That is, we create a controlled time-varying phase difference between the collimated light beam polarization components before entering the conoscopic part of the setup. As a result, the fringe pattern collected is phase modulated according to the retardance introduced. The fringe movement allows the identification of both the fast and the slow axes, and the determination of the retardance introduced. In this section, we show how it is possible to characterize a retarder under study

at a given wavelength by means of a laser source, a uniaxial crystal, polarizer sheets, and a CCD [23] or a photodetector array.

There are different techniques for identifying the fast and slow axes as well as the retardance of a wave plate [24–29]. Finding the principal axes is in general an easy task. Malus law indicates that, given a linearly polarized source, if we rotate a linear polarizer (analyzer) azimuthally in front of a detector, we obtain a sinusoid. In a complete turn, two maxima and two minima are obtained when the transmission axis is parallel and perpendicular to the plane of polarization of the incident light, respectively. If we place a wave plate before the analyzer, the alignment of one of its axes (either the fast or the slow axis) with the original plane of polarization leads to the same location of the two pairs of maxima and minima. This way, it is possible to identify the angular location of both principal axes of the retarder. However, we cannot assure which of them corresponds to the fast axis and which one to the slow axis. In order to solve this, we propose to measure the phase difference between two fixed orthogonal components of the electric field (v and h) that exits the rotating wave plate by means of the phase demodulator discussed in previous sections.

A. Wave Plate Azimuth Rotation

The retardance introduced between two components of the electric field (v and h) may be modified by rotating a wave plate in front of a polarized monochromatic source of light. In this case, we measure the retardance introduced by a wave plate as a function of the azimuth rotation angle. We employ a lab frame (x, v, h), where x corresponds to the direction of incidence, v corresponds to the vertical axis, and h to the horizontal axis. The incident wave is linearly polarized at 45° from the v and h axes (Fig. 4). Thus, the v and h components of the incident field have the same phase and amplitude. By means of simple Jones calculus, we can obtain the phase shift $\Delta\phi_{v-h}(\Omega)$ introduced by a wave plate of retardance $\Delta\phi_{\mathrm{WP}}$ as a function of the azimuth angle Ω (Fig. 4)

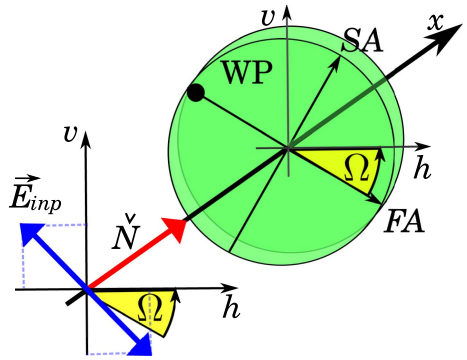

Fig. 4. Incident electric field polarized at 45° from the v and h axes. FA corresponds to the fast axis, and SA corresponds to the slow axis.

$$\Delta\phi_{v-h}(\Omega) = \arctan\left[\frac{2\cos 2\Omega \sin \Delta\phi_{\mathrm{WP}}}{(\cos 4\Omega + 1)(\cos \Delta\phi_{\mathrm{WP}} - 1) + 2}\right]. \tag{16}$$

It is worth noting that $\Delta\phi_{\mathrm{WP}}$ should be expressed in π modulus like most commercial retarders (e.g., for a quarter-wave retarder, $\lambda/4$ corresponds to $\Delta\phi_{\mathrm{WP}} = \pi/2$) and $-\Delta\phi_{\mathrm{WP}} < \Delta\phi_{v-h}(\Omega) < \Delta\phi_{\mathrm{WP}}$. If we place the wave plate between the first polarizer of Fig. 1 and the crystal plane-parallel plate, it would act as a phase modulator. When the fast axis is aligned with the vertical axis, the slow axis is horizontal. This way, according to the above definition, $\Delta\phi_{v-h}(\Omega)$ reaches a minimum. In turn, if the slow axis is vertical, the fast axis is horizontal and $\Delta\phi_{v-h}(\Omega)$ reaches a maximum. However, in both cases, the reached extrema are the same magnitude. Then, the intention is using the polarization interferometer previously described as a phase analyzer to track the phase variations corresponding to $\Delta\phi_{v-h}(\Omega)$. If dealing with a quarter-wave plate, the phase shift between the v and h components varies between −90° and 90°. These extrema are respectively reached when the fast axis is parallel to the h axis and to the v axis. In both cases, this leads to circular polarization with different handedness. When the fast axis and the slow axis are at 45° from the v and h axes, the polarization state is linear (and also the same as the incident polarization state). For the remaining orientations, the polarization state is elliptical.

B. Experiment

We evaluate the techniques presented in Section 3 by means of the quartz plate that gives the interference patterns of Fig. 2. Since the fringes at a plane of coordinates (x_D, y, z) depend on $\Delta\phi(\vec{\mathbf{r}}, t) = \Delta\phi_{o-e}(y, z) + \Delta\phi_{v-h}(\Omega)$, they would move laterally according to $\Delta\phi_{v-h}(\Omega)$ [Eq. (16)].

We employ a $\lambda_v = 543.5$ nm He–Ne laser and two different detection systems: a CCD camera associated with the phase recovery technique described in Subsection 3.A and an *ad hoc* photodiode array for the technique described in Subsection 3.B. For both methods, we perform intensity measurements at turn intervals of 2°.

In the case of the method of Subsection 3.A, we capture a series of interferograms that allows the recovery the phase $\Delta\phi_{o-e}(y, z) + \Delta\phi_{v-h}(\Omega)$ for each of them. Since the phase introduced by the polarization interferometer $\Delta\phi_{o-e}(y, z)$ remains constant for every turn, we can recover $\Delta\phi_{v-h}(\Omega)$. As mentioned before (Subsection 4.A), if the wave plate is perfectly rotated around the normal to the surfaces, $\Delta\phi_{v-h}(\Omega)$ varies between a maximum and a minimum of the same magnitude. Thus, the retardance $\Delta\phi_{\mathrm{WP}}$ of the wave plate corresponds to half the phase difference between both peaks.

A rise in $\Delta\phi_{v-h}$ corresponds to a rise in $\Delta\phi_{o-e}(y, z) + \Delta\phi_{v-h}(\Omega)$ since $\Delta\phi_{o-e}(y, z)$ remains unaltered. This can be observed as a displacement of the vertical

fringes of the interference pattern to the right side (Fig. 2). This way, we can identify the fast axis and the slow axis of the wave plate. If we rotate the wave plate as the fast axis approaches the horizontal axis, the fringes move rightward until they reach a maximum displacement when both axes are parallel (blue squares, Fig. 5). If we continue rotating the wave plate, the direction of the displacement is reversed and the fringes move leftward (green circles, Fig. 5) until they reach a maximum displacement when the fast axis is vertical (red crosses, Fig. 5).

Having the identification of the axes allows us to perform a wide range of experiments. Despite the fact that the phase shift introduced by the wave plate can be calculated by measuring the polarization ellipse, current experimental setups also allow it. That is, it is possible to take advantage of the fringe displacement in order to calculate the phase shift $\Delta\phi_{\mathrm{WP}}$ for the employed wavelength.

In order to accomplish the wave plate characterization by means of the spatial phase stepping technique (Subsection 3.B) we employ three photodiodes and a three-step algorithm. The photodiodes were distributed along the detection plane $x = x_D$, and by means of a linear modulation performed by a birefringent phase shifter, we normalize the photodiode means and amplitudes [related to $a(x_D, y_i, z_i)$ and $b(x_D, y_i, z_i)$ of Eq. (14)] and also adjust their relative phase shift to $\pi/2$.

Figure 6 shows the results obtained by means of the two methods proposed here and a theoretical calculation of the phase shift $\Delta\phi_{v-h}(\Omega)$ introduced by a quarter-wave plate.

The retardance of the wave plate $\Delta\phi_{\mathrm{WP}}$ is approximately $\pi/2$ for $\lambda_v = 543.5$ nm according to criterion previously discussed. The theoretical line (black solid line, Fig. 6) allows us to the appreciate some systematic errors associated with the experiment. However, the results obtained by means of both methods and

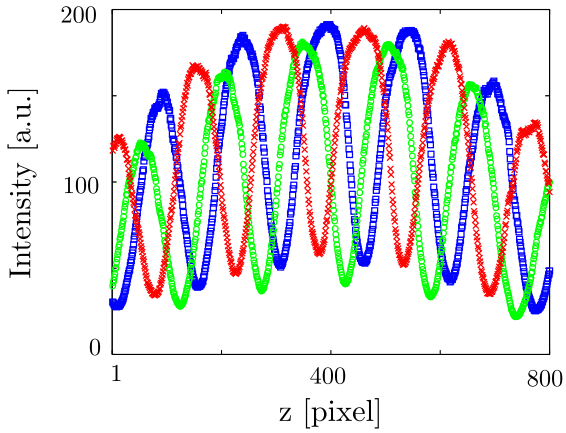

Fig. 5. 1D fringe movement (intensity average along columns). The blue squares correspond to the fast axis when placed horizontally (angle of rotation 14°), the green circles correspond to a point in the middle (angle of rotation 60°), and the red crosses correspond to the fast axis when placed vertically (angle of rotation 104°).

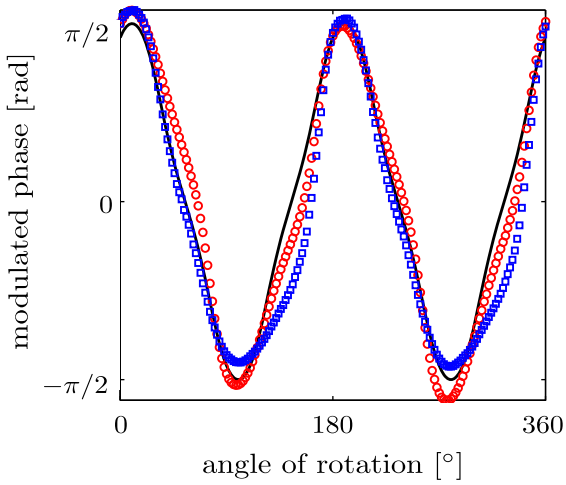

Fig. 6. Phase modulated by a rotating quarter-wave retarder as a function of the angle of rotation. Red circles correspond to the phase estimation by means of the Fourier transform method and a digital camera (Subsection 3.A). Blue squares correspond to the phase shifting estimation performed with a three-photodiode linear array (Subsection 3.B). Black solid line corresponds to the theoretical calculation of an ideal rotation of a quarter-wave retarder.

the theoretical model of Eq. (16) are comparable. The differences between the theoretical model, associated with a perfect rotation of a quarter-wave plate, and the FTM (Subsection 3.A) are mainly due to the lack of coincidence of the rotation axis and the normal to the wave plate. In the case of the simultaneous phase stepping technique (Subsection 3.B), there is an additional difference due to the decalibration of the phase steps between the photodetectors.

Even though we apply modest processing techniques that require minimal hardware and software capabilities, we obtain good results. In addition, the higher the number of photodetectors, the more robust the system. We evaluate almost at the limit where the estimation of the carrier frequency k_{z0} is easy to find by means of a CCD (i.e., a large number of photodetectors). When the number of photodiodes is smaller, the estimation of k_{z0} is harder, and extreme care should be taken in positioning them. However, it is possible to employ self-calibrating algorithms and take advantage of the quasi-linear phase distribution of the quartz crystal employed [30].

5. Conclusions

We proposed to employ uniaxial crystals as phase demodulators for time-dependent phase unknowns. The modulating system or modulator is required to introduce a phase variation between orthogonal components of the electric field of a laser beam. Distinct techniques and modulators, that comply with this, can be implemented, such as polarized Michelson or Mach–Zehnder interferometers as well as birefringent interferometers of different kinds and for different purposes. Finally, the modulated light goes through a polarization interferometer consisting of a plane-parallel uniaxial plate. One of the main

features of this plate is its ability to hold a constant (time-invariant) phase distribution over the detection plane. This birefringent crystal used for conoscopy may not need to be accurately cut. In the case of the method described in Subsection 3.A, it is only necessary for the birefringent plate to provide interferograms with a distinguishable spatial carrier. For quartz, this condition is achievable if the optical axis is close to 45° from the interfaces. However, tolerances can also be deeply studied by means of Eqs. (2)–(6) [4].

The case study presented here corresponds to a wave plate characterization, which is very important for polarization control, and allows the comparison between two different techniques that employ the same working principle. Although the wave plate characterization presented here is a useful and inexpensive laboratory practice, the demodulator itself is also of great interest. However, some of its capabilities have not been fully tested. The implementation with fewer detectors proposed here leads to a potentially faster demodulator. Since there is no temporal carrier frequency, the complete bandwidth of the photodetector and amplifier can be exploited. Therefore, the demodulator bandwidth is increased, allowing it to track faster signals.

The results obtained here are based on a robust common path crystal interferometer that leads to the future development of a different field of phase estimation. However, the usual ambitions are still the goals to achieve: accuracy, resolution, speed, etc. Different applications in a variety of disciplines such as ultrasonics and communications as well as handheld field equipment can benefit from its capabilities.

This work was supported by a postdoctoral grant and a PIP grant (2012–2014 11220110100241CO) from CONICET, and two UBACYT grants from Universidad de Buenos Aires (UBACYT 2013–2016 20020120100025BA and UBACYT 2014–2017 20020130100346BA).

References

1. R. M. A. Azzam and N. Bashara, *Ellipsometry and Polarized Light* (North-Holland Physics, 1988).
2. M. Takeda, "Fourier fringe analysis and its application to metrology of extreme physical phenomena: a review," Appl. Opt. **52**, 20–29 (2013).
3. J. C. Wyant, "Computerized interferometric surface measurements," Appl. Opt. **52**, 1–8 (2013).
4. F. E. Veiras, M. T. Garea, and L. I. Perez, "Wide angle conoscopic interference patterns in uniaxial crystals," Appl. Opt. **51**, 3081–3090 (2012).
5. O. Pikoul, "Determination of the optical sign of a crystal by a conoscopic method," J. Appl. Crystallogr. **43**, 955–958 (2010).
6. S. Jen and C. S. Hartmann, "Conoscope: an apparatus for determining crystal orientation of saw wafers," in *Proceedings of IEEE Ultrasonics Symposium* (IEEE, 1994), Vol. **1**, pp. 397–401.
7. P. Ayras, A. T. Friberg, M. Kaivola, and M. M. Salomaa, "Conoscopic interferometry of wafers for surface-acoustic wave devices," J. Appl. Phys. **82**, 4039–4042 (1997).
8. P. H. Äyräs, A. T. Friberg, M. A. J. Kaivola, and M. M. Salomaa, "Conoscopic interferometry of surface-acoustic-wave substrate crystals," Appl. Opt. **38**, 5399–5407 (1999).
9. B. L. V. Horn and H. H. Winter, "Analysis of the conoscopic measurement for uniaxial liquid-crystal tilt angles," Appl. Opt. **40**, 2089–2094 (2001).
10. Y. Malet and G. Y. Sirat, "Une application de l'holographie conocopique: des telemetres a usages multiples," J. Opt. **29**, 183–187 (1998).
11. I. Álvarez, J. M. Enguita, M. Frade, J. Marina, and G. Ojea, "On-line metrology with conoscopic holography: beyond triangulation," Sensors **9**, 7021–7037 (2009).
12. C. Oh, S. O. Isikman, B. Khademhosseinieh, and A. Ozcan, "On-chip differential interference contrast microscopy using lensless digital holography," Opt. Express **18**, 4717–4726 (2010).
13. M. M. Brundavanam, Y. Miyamoto, R. K. Singh, D. N. Naik, M. Takeda, and K. Nakagawa, "Interferometer setup for the observation of polarization structure near the unfolding point of an optical vortex beam in a birefringent crystal," Opt. Express **20**, 13573–13581 (2012).
14. M. Takeda, H. Ina, and S. Kobayashi, "Fourier-transform method of fringe-pattern analysis for computer-based topography and interferometry," J. Opt. Soc. Am. **72**, 156–160 (1982).
15. P. K. Rastogi, *Holographic Interferometry*, 1st ed. (Springer-Verlag, 1994).
16. B. V. Dorrío and J. L. Fernández, "Phase-evaluation methods in whole-field optical measurement techniques," Meas. Sci. Technol. **10**, R33–R55 (1999).
17. P. K. Rastogi, *Photomechanics*, 1st ed. (Springer-Verlag, 2000).
18. P. Jacquot, "Speckle interferometry: a review of the principal methods in use for experimental mechanics applications," Strain **44**, 57–69 (2008).
19. G. H. Kaufmann, A. E. Ennos, B. Gale, and D. J. Pugh, "An electro-optical read-out system for analysis of speckle photographs," J. Phys. E **13**, 579–584 (1980).
20. G. Kaufmann, "On the numerical processing of speckle photograph fringes," Opt. Laser Technol. **12**, 207–209 (1980).
21. S. A. Isacson and G. H. Kaufmann, "Two-dimensional digital processing of speckle photography fringes. 1: diffraction halo influence for the noise-free case," Appl. Opt. **24**, 189–193 (1985).
22. C. J. Morgan, "Least-squares estimation in phase-measurement interferometry," Opt. Lett. **7**, 368–370 (1982).
23. F. E. Veiras, L. I. Perez, M. T. Garea, and L. M. Riobó, "Simple technique for determining the wave plate's fast axis and retardance," presented at the Eighth Iberoamerican Conference on Optics and the Eleventh Latin American Meeting on Optics, Lasers and Applications, Porto, Portugal, 2013.
24. M.-H. Chiu, C.-D. Chen, and D.-C. Su, "Method for determining the fast axis and phase retardation of a wave plate," J. Opt. Soc. Am. A **13**, 1924–1929 (1996).
25. D.-C. Su and C.-C. Hsu, "Method for determining the optical axis and (ne, no) of a birefringent crystal," Appl. Opt. **41**, 3936–3940 (2002).
26. C.-C. Tsai, H.-C. Wei, C.-H. Hsieh, J.-S. Wu, C.-E. Lin, and C. Chou, "Linear birefringence parameters determination of a multi-order wave plate via phase detection at large oblique incidence angles," Opt. Commun. **281**, 3036–3041 (2008).
27. W. Liu, M. Liu, and S. Zhang, "Method for the measurement of phase retardation of any wave plate with high precision," Appl. Opt. **47**, 5562–5569 (2008).
28. Y. Zhang, F. Song, H. Li, and X. Yang, "Precise measurement of optical phase retardation of a wave plate using modulated-polarized light," Appl. Opt. **49**, 5837–5843 (2010).
29. W. Chen, H. Li, S. Zhang, and X. Long, "Measurement of phase retardation of waveplate online based on laser feedback," Rev. Sci. Instrum. **83**, 013101 (2012).
30. P. Carré, "Installation et utilisation du comparateur photoélectrique et interférentiel du bureau international des poids et mesures," Metrologia **2**, 13–23 (1966).